AD-A086 727 NAVAL RESEARCH LAB WASHINGTON DC F/G 20/9
PROPERTIES OF ABLATIVELY ACCELERATED TARGETS.(U)
MAY 80 B H RIPIN, S E BODNER, S H GOLD
UNCLASSIFIED NRL-MR-4212 SBIE-AD-E000 456 NL

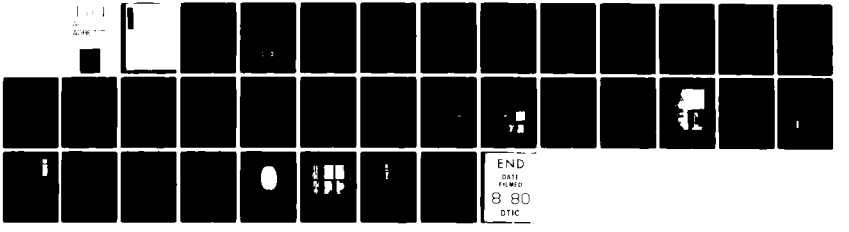

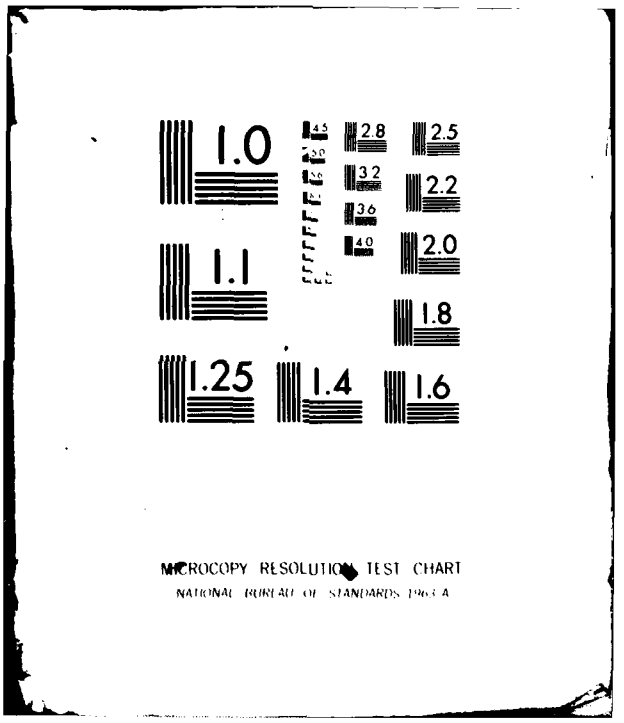
1.0
1.1
1.25
1.4
1.6
1.8
2.0
2.2
2.5
2.8
3.2
3.6
4.0
MICROCOPY RESOLUTION TEST CHART
NATIONAL BUREAU OF STANDARDS 1963 A

SECURITY CLASSIFICATION OF THIS PAGE (When Data Entered)

REPORT DOCUMENTATION PAGE

READ INSTRUCTIONS BEFORE COMPLETING FORM

1. REPORT NUMBER: NRL Memorandum Report 4212	2. GOVT ACCESSION NO.: AD-A086727
3. RECIPIENT'S CATALOG NUMBER:	
4. TITLE (and Subtitle): PROPERTIES OF ABLATIVELY ACCELERATED TARGETS	5. TYPE OF REPORT & PERIOD COVERED: A continuing report
	6. PERFORMING ORG. REPORT NUMBER:
7. AUTHOR(s): B.H. Ripin, S.E. Bodner, S.H. Gold, H.R. Griem*, J. Grun*, M.J. Herbst†, R.H. Lehmberg, E.A. McLean, J.M. McMahon, S.P. Obenschain, J.A. Stamper, R.R. Whitlock, and F.C. Young	8. CONTRACT OR GRANT NUMBER(s): 1707319.1401
9. PERFORMING ORGANIZATION NAME AND ADDRESS: Naval Research Laboratory, Washington, D.C. 20375	10. PROGRAM ELEMENT, PROJECT, TASK AREA & WORK UNIT NUMBERS: 61153N; RR011-09-41; 67-0859-A-0
11. CONTROLLING OFFICE NAME AND ADDRESS: U.S. Department of Energy, Washington, D.C. 20545	12. REPORT DATE: May 16, 1980
	13. NUMBER OF PAGES: 33
14. MONITORING AGENCY NAME & ADDRESS (if different from Controlling Office)	15. SECURITY CLASS. (of this report): UNCLASSIFIED
	15a. DECLASSIFICATION/DOWNGRADING SCHEDULE:

16. DISTRIBUTION STATEMENT (of this Report)

Approved for public release; distribution unlimited.

17. DISTRIBUTION STATEMENT (of the abstract entered in Block 20, if different from Report)

18. SUPPLEMENTARY NOTES

First submitted as an invited paper at the CLEOS/ICF'80 Topical Meeting on Inertial Confinement Fusion, February 27, 1980, San Diego, California.

*Present address: University of Maryland, College Park, Maryland.
†Present address: Mission Research Corporation, Alexandria, Virginia.

19. KEY WORDS (Continue on reverse side if necessary and identify by block number)

Laser-fusion	Acceleration
Ablation	Hydro-efficiency
Laser-plasma	Symmetry
Heat-transport	Rayleigh-Taylor

10 to the 7th power

20. ABSTRACT (Continue on reverse side if necessary and identify by block number)

Targets are ablatively accelerated to high velocity ($>10^7$ cm/s) with good hydrodynamic efficiency (~20%) using low-irradiance (10^{13} - 10^{14} W/cm^2) long (3 - 4 ns) Nd-laser pulses. Detailed properties of the interaction and acceleration as well as comments upon the suitability of this approach to the laser fusion application are presented. Results of unique "double-target" experiments are also included.

10 to the 14th power
10 to the 13th power

DD FORM 1 JAN 73 1473 EDITION OF 1 NOV 65 IS OBSOLETE
S/N 0102-LF-014-6601

SECURITY CLASSIFICATION OF THIS PAGE (When Data Entered)

CONTENTS

PROPERTIES OF ABLATIVELY ACCELERATED TARGETS

I. Introduction:

The essence of our approach towards laser fusion at the Naval Research Laboratory is depicted in the cartoon shown in Fig. 1. Laser-plasma experiments done at high-irradiance by us and others have elucidated a number of physics results which are not favorable to laser fusion. Among these "devilish" effects which are forcing us to lower irradiance are Brillouin backscatter,[1] preheat from energetic electrons,[2] poor driver and hydrodynamic efficiencies and poor heat transport.[3] On the other hand, too low an irradiance may cause trouble through hydrodynamic instability. We are trying to find an "irradiance window" acceptable to laser fusion between the devil and the deep blue sea. Hopefully, there is such a window.

The experiments that will be described are directed towards the stable acceleration of planar foils and discs to speeds thought to be required to initiate pellet ignition (2×10^7 cm/sec) with good overall efficiency and on a low adiabat (low preheat).[4] (Fig. 2). We use planar targets in our experiments which can be thought of as a small section of a larger pellet surface before convergence effects become important. This affords rear surface diagnostic and interpretational simplicity. The focal diameter requirement will be discussed later. We are investigating the long-pulse, 10^{13} - 10^{14} W/cm^2 laser regime which may contain the sought after window at 1.05μm wavelength.

The stages of the ablative acceleration process,shown in Fig. 3, will be discussed in this paper approximately in the order in which they occur. That is, first the laser energy is absorbed near the critical surface. This energy then flows towards the ablation surface where material is ablated (blown-off) much as is a rocket exhaust, and the

Manuscript submitted April 9, 1980.

target is accelerated forward. Eventually the target either reaches the final desired speed and condition or irradiation non-uniformity and hydrostability effects manifest themselves. It is important to note that when we say ablative acceleration we mean the continuous rocket-like acceleration of the target due to the plasma blow-off. This is not an explosive acceleration such as in exploding pusher targets or as in targets with thick walls where the outer layer is exploded away and the colder inner portion reacts impulsively. Here we will review experimental results on the ablative acceleration process, reported previously by us, and then describe material which has not yet been presented elsewhere.

II. Experimental description:

The driver for the experiments is the Pharos II Nd-phosphate laser which is summarized in Fig. 4. The laser is described elsewhere by J.M. McMahon.[5] The most important features of Pharos II in regard to the experiments described here are that it delivers more than 200 J in 3-4 nanoseconds with a fairly flat-topped uniform focal distribution of 1-mm diameter and of order 10^{13} W/cm^2 irradiance.

The experiment is shown schematically in Fig. 5. The incident beam is, of course, well-diagnosed: the energy, temporal behavior and spatial properties of the focal distribution are measured on each shot. The laser light is focused onto the targets with an f/6, 1.2m focal length lens. The target is placed in the near-field of the lens so as to achieve the most uniform possible irradiation with about 1-mm diameter focal spot. Absorption and asymptotic plasma properties are measured several ways including: a box calorimeter with and without an ion shield; arrays of paired miniature calorimeters, one accepting light and the other all emissions; a time-of-flight

ion detector array for velocity information; and a ballistic pendula array for direct momentum measurement. Heat transport, both axial and lateral, is investigated using a variety of x-ray diagnostics and techniques. Time-resolved measurements of the acceleration process before, during and after the incident laser pulse strikes the target are made using a frequency doubled, 527-nm, optical probe beam of duration 0.3 nsec via interferometry, shadowgraphy, and a temporally stretched probe for streak photography. Probe light is sometimes reflected from the target rear to obtain its velocity across a diameter via a Doppler shift measurement.[6] In addition, other special techniques are used, for example, to obtain the temperature of the target rear (from time-resolved blackbody emission measurements),[7] to obtain the density distribution within the accelerating target (double-target experiments), or to obtain ablation rates and axial heat transport (layered targets),[8] or illumination uniformity requirements (coded lens' apertures).[8] These techniques will be described later in this report. Most properties are diagnosed in a multiplicity of ways to insure self-consistency and to give confidence in the results.

III. Absorption:

The laser absorption properties have been described elsewhere[4,8] so here we summarize just the major results. (Fig. 6). The basic finding is that for 3-nanosecond pulses at low-irradiance, i.e., 10^{12} to a few times 10^{13} W/cm^2, the absorptions are high at values of about 80% to 90%.[8,9] As irradiance increases above 10^{14} W/cm^2 range, absorption is seen to decrease. At low-irradiance the absorbed energy appears predominantly thermal in character. This is seen in Fig. 7 which shows three x-ray spectra at different incident irradiances. All three spectra show a

slope consistent with a 250-300 eV temperature in the 1-4 keV portion of the x-ray spectra. The cases at about 10^{13} W/cm^2 and below exhibit minimal high energy tails (hot electrons), indicating that absorption is predominantly thermal. As the incident laser irradiance is increased, the hot-electron tail increases up to values comparable to those found in high-irradiance experiments. The point is, however, that at low-irradiance where we hope to find the irradiance window, the laser absorption is excellent and predominantly thermal. This is desirable for the laser fusion application.

IV. Ablative Acceleration:

Now we will address the ablation and acceleration properties of the target. Fig. 8 shows interferometric and shadowgraphic optical views of the target during the acceleration process, along with the applied focal distribution. The probe pulse is passed tangential to the target surface at various times indicated relative to the peak of the incident laser pulse. The iso-intensity contours within the focal distribution differ by 0.4. Note that the focal spot is relatively flat-topped, 1-mm diameter and has about $\pm$50% non-uniformity. The blow-off plasma (ablation plasma) goes off to the left and one can see the target react and accelerate to the right. The interferogram shows a well-defined planar slug of material with little plasma (lack of fringe bending) beyond it. The dual-time shadowgrams taken on the same shot indicate a velocity of about 10^7 cm/sec. At the later times shown the target has been accelerated by more than 70 times its original thickness, crudely corresponding to an aspect ratio of 70, without evidence of gross breakup. No front side hot plasma was found on the rear, nor jets, etc. A fuzzy rear surface is noticeable in the shadowgrams at late times but its origin

is not known at the moment. Possible explanations include: an optical artifact, fluff, or possibly the result of very short wavelength hydrodynamic instability.

Let's now review some of our observations of the asymptotic ablative acceleration process.[10] The angular distribution of the energy and velocity distribution of ablating plasma and accelerated target is shown on the right and left sides of the target foil in Fig. 9. The ablated plasma exhibits the well-defined ablation velocity peak first discussed by Sandia.[11] All species and ionization states are ablated with nearly the same velocity because ion-ion collision rates are high enough above 10^{19} cm^{-3} density to cause the ablated plasma to behave as a single fluid. The average ablation velocity and target velocity are obtained from these curves. The hydrodynamic efficiency, η_h, i.e., the accelerated target energy divided by the total absorbed energy, is obtained by integrating the energy angular distributions. The ablated mass fraction, $\Delta m/m$, is obtained from the integral of the $2E/u^2$ distributions. Results obtained in this manner are plotted in Fig. 10 along with predictions of η_h and $\Delta m/m$ from the simple, 1-D, steady-state rocket model. The targets are CH foils irradiated at 5×10^{12} - 10^{13} W/cm^2. The rocket model predicts a peak efficiency of 65% when the ablation velocity, u, and final target velocity, v, are comparable. The experimental results for η_h fall below this optimistic prediction due to the fact that the experiment is not completely one-dimensional. However, values of η_h greater than 20% are seen routinely for targets accelerated to speeds of $1\text{-}2 \times 10^7$ cm/sec. These results are seen to be insensitive to the irradiation spot diameter. Efficiencies this high are favorable to the laser fusion application.

Experiments have been conducted to ensure that laser irradiation spot size is sufficiently large so that edge effects are relatively unimportant.[12] Although the predictions of the simple rocket model are not affected, the lateral leakage of energy out of the edges does affect the ablation velocity, mass ablation rates, energy partition, and uniformity of the acceleration. Fig. 11 shows the dependence of the average ablation velocity with the irradiation diameter at constant irradiance. Analogous results are found at higher irradiances also. It is seen that 1-mm spot diameters are sufficiently close to the asymptotic ablation velocity to ignore edge effects. Large targets also allow study of long wavelength uniformity and stability requirements.

Ablation velocity is not a strong function of irradiance, I, as shown in Fig. 12, increasing as $I^{0.3}$. This remains true until, in the mid-10^{14} W/cm^2 range, fast ions appear and degrade the ablation process. Ablation velocity is an important parameter since, for a given desired final target velocity, it determines the highest hydrodynamic efficiency that can be achieved. The fact that it does not increase strongly with irradiance gives some flexibility in the final choice of irradiance.

Ablation pressure, P, is another important parameter since this determines the rate of target acceleration. Pressure can be expressed and inferred experimentally in several ways. For example,

$$P = \begin{cases} \dot{m}u_\perp/A & \text{(a)} \\ 2I_a u_\perp^2/u & \text{(b)} \\ m\dot{v}/A & \text{(c)} \\ P_\perp/\tau_\ell A & \text{(d)} \end{cases} \qquad (1)$$

The first three relations are modifications of one-dimensional treatments to account for two-dimensional effect.

Measurements of the target and ablation momentum allow a determination of the pressure using Eq. (1d). The parameters in Eq. (1d) are: $p_\perp$ the integrated normal component of the momentum; τ_ℓ the laser pulse duration; and A the area of the irradiated disc. A picture and description of a type of ballistic pendulum, used to make direct total momentum measurements, is shown in Fig. 13. Arrays of these pendula have been placed on both sides of the target, and, on some shots, the target itself is mounted on the totally capturing pendulum of Fig. 13. Typical results are shown in Fig. 14. Momentum is conserved in these experiments and the absolute calibration factors of the pendula are known. Pressure versus absorbed irradiance is shown in Fig. 15 for several CH disc target diameters. Multi-megabar pressures are evident with a $I_a^{0.9}$ dependence upon absorbed irradiance I_a. Another method to obtain the momentum, to be inserted in Eq. (1d) to infer the pressure, is to use $p_\perp = 2(E/u)_\perp$, i.e., the angular distribution of plasma energy E divided by the velocity in the plasma blowoff times cos θ and averaged over all solid angles. Both these methods agree to better than 30%.[13] Estimates of pressure using Eqs. (1a)-(1c) also agree with these data within a factor-of-two.

Estimates of the mass ablation rate can also be made by several methods. We, in fact, strive in our experiments to obtain as many independent measures as possible of all observables to check for consistency. In addition to the usual measures of $\dot{m}$ by, for example, dividing the observed ablated mass by the pulse duration, looking at the time-resolved response of the target, etc., we also obtain $\dot{m}$ from time-integrated and time-resolved layered target experiments. The method has been used previously[3,8] and its logic is outlined in Fig. 16. Aluminum line radiation

in the 1 to 2 keV region is typically 10^2-times more intense than CH emission when heated to a few-hundred electron volts. By placing CH over an Aℓ target and observing the intensity and temporal x-ray emission dependence upon CH layer thickness, the thickness of CH ablated per unit time can be estimated. Such data at two irradiances are shown in Fig. 17. One sees the magnitude of the x-ray signal increases rapidly for CH-layer thicknesses less than 0.6μm and 2μm at irradiances of 2×10^{12} W/cm^2 and 10^{13} W/cm^2 (spot diameter = 230μm) which, when divided by the 3-nsec pulse duration, gives CH mass ablation rates of 0.06 and 0.2 gm/cm^2-nsec, respectively. From the time-resolved x-ray traces shown on the right side of Fig. 17 one sees the delayed enhanced x-ray emission when the heat finally reaches the Aℓ substrate after ablating the 2μm layer of CH late in the laser pulse (at 10^{13} W/cm^2). The delayed emission precludes hot electron or x-ray heating of the substrate. The target appears to be peeled like an onion by the ablation process.

V. Rear Surface Temperature:

Eventually, the heat from the hot front (ablating) side of the target reaches the cold rear surface. Measurements of the temporal history of the target rear temperature leads to estimates of the fuel preheat and isentrope, and, hopefully, an understanding of heat transport mechanisms into the target.[7] Time-resolved rear surface temperatures are found by measuring the absolute intensity of the visible continuum at several wavelengths, using the arrangement shown in Fig. 18, and relating them to blackbody emission. Approximately one-nanosecond time resolution is obtained in this apparatus. Some of these peak intensity data are plotted in Fig. 19 versus wavelength. Both data and blackbody curves are absolute.

Note the good agreement in magnitude (brightness-temperature) and shape (color-temperature). Note also that the thicker the target the lower the peak temperature on the rear surface. The time history of the rear surface temperature is illustrated in Fig. 20. Here it is seen that the heat reaches the target rear surface late in the laser pulse and the temperature rise is delayed with increasing target thickness. The mode of heat transport causing this temperature rise is still not uniquely determined and such processes as thermal conduction, shock wave heating, fast electrons and radiant heating are being considered.[14] Although the observed temperatures between 0.5 and 20 eV may affect the present experiments, they are not alarmingly large for the laser fusion application since the reactor sized pellets will have much thicker walls than these present targets which should better insulate the fuel.

IV. Uniformity Requirements:

We have shown up to this point that the physics looks attractive for a low-irradiance long-pulse approach to laser fusion: the absorption and hydrodynamic efficiencies are very high; the energy is absorbed predominantly thermally, the target acceleration is ablative with final velocities greater than 10^7 cm/sec, i.e., nearly the required speed, and preheat is low. A crucial issue that remains is what <u>illumination</u> uniformity (or, target uniformity) is needed to achieve the one-percent or so <u>pressure</u> uniformity at the ablation surface required to do a high-convergence compression of a pellet? Some of the considerations involved in this question are illustrated in Fig. 21. Hot-spots in the driver irradiation (or target imperfections) cause kinematic non-uniform accelerations due to ablation pressure and local mass ablation rate variations. These variations may be further aggravated by growth of

Rayleigh-Taylor hydrodynamic instability. Thermal conduction tends to wash out these hot spots by diffusion of heat between the absorption region, n_c, and the ablation surface, n_a. The better the lateral thermal conduction, the less effect the hot spots have on the acceleration. Also, the better the axial thermal conduction, the larger is the separation between n_c and n_a and hence longer wavelength non-uniformities can be washed out. Some tests of the effect of incident beam non-uniformities upon the accelerating target velocity profile are shown in Figs. 22 and 23. The technique used here to measure the velocity profile across the target rear is to measure the Doppler shift of a short-duration (0.3 nsec) probe pulse reflected off of the rear target surface into a stigmatic spectrograph.[6] Fig. 22 shows two such profiles taken at the peak of the laser pulse along with the associated irradiation intensity profile. A relatively well-behaved irradiation profile (top) yields a well-behaved velocity profile. In the example on the bottom of Fig. 22, however, we impressed a 6:1 incident intensity variation separated by about 100μm on the target by placing a crude coded aperture (strip of paper) across the focusing lens. The resulting target velocity profile showed about 2:1 corresponding variations. Thus, some wash out of impressed irradiation nonuniformity is accomplished on 100-μm lateral scale implying that the distance between n_c and n_a is also the-order-of 100μm.[4,8,15] Fig. 23 shows another example, but with a 1-mm laser spot diameter, along with an x-ray pinhole photo densitometer trace across the corresponding target diameter.

VII. Double-target experiments:

There is great need of a technique which can diagnose the high-

density region of the target on a time-resolved basis. X-ray backlighting is one approach which shows great promise of doing these measurements. However, our backlighting experiments are in the formative stage so we tried another technique, that of using double-targets to obtain much the same information. The double-target experimental technique is illustrated in Fig. 24. A second target (impact plate) is placed behind the accelerating first foil. Upon impact the second target responds much as a miniature ballistic pendulum and its resulting motion gives information about the irradiated target. By choice of mass, thickness and spacing of the two foils, the technique can act: as a planar analogue to a double-shell pellet in velocity multiplication experiments, as a diagnostic of the first target's properties, or to create high-pressures by quickly dumping the momentum built up over a long acceleration period of the first-target onto the second-target. Here, we will only discuss some recent experiments in the diagnostic mode. Fig. 25 illustrates the principle behind these experiments. The blobs of accelerated plasma, as seen for example in the interferograms of Fig. 8, may contain a density profile as sketched in Fig. 25, that is, a low density precursor region followed by a well-defined and localized high density region. When this profile hits the second (diagnostic) target it responds to the applied pressure as $P_1(t) \approx \rho_1 v_1^2 \simeq m_2 \dot{v}_2$. By observing the time-resolved acceleration of the second target with, for example, a streak camera or framing photography, or with the Doppler shift technique previously described, the density and pressure profiles of the laser accelerated material can be deduced. Until the exact nature (elastic vs. inelastic, etc.) of the collision is determined these estimates are good to about a factor-of-two. Fig. 26

shows a double-disc target before irradiation. Fig. 27 shows a representative shot with a double-foil (top) and corresponding single-foil (bottom) at three-times with respect to the peak of the laser pulse, i.e., before, +9 nsec, and +11.5 nsec. Note that the stagnation of the first foil against the second at 9 nsec implies that a low density precursor rides ahead of the high density region. Another example of a double-foil shot which shows similar behavior, but perhaps more clearly, via streak photography is shown in Fig. 28. The irradiation conditions and geometry are shown on top, a before-shot streak-shadowgram (0.53μm) photo showing the location of the two foils and timing markers in the middle, and the actual shot on the bottom. One sees the first foil accelerate during the incident laser pulse and strike the second foil. A dwell period follows in which the second foil does not respond. This again implies a very low density precursor in front of the main target mass. Finally, the second-foil apparently accelerates to full speed within one-nanosecond implying a very well-defined and localized high-density region in the accelerated target. (As an aside, note that the front surface of the second-target foil is slowly expanding before being struck by the first-target perhaps due to radiant heating by the first target.)

VIII. Conclusions:

The major benefits of a low-irradiance (10^{13} - 10^{14} W/cm^2), long-pulse (multi-nsec) approach to laser fusion are enumerated in Fig. 29. High driver, absorption, and hydrodynamic efficiencies are demonstrated. The driver pulse, laser or whatever, can be relatively unshaped and the

reactor pellets relatively simple. The physics issues addressed thus far look attractive: the absorption is efficient (~80%) and predominantly thermal (250-300 eV). Preheat is low (~few eV) and continuous ablative acceleration works well with demonstrated final target velocities above 1×10^7 cm/sec and high hydrodynamic efficiencies (≳20%) without gross breakup of the target. We showed that small scale (less than 100μm) incident nonuniformities tend to get washed out at the ablation surface via lateral thermal conduction. Also, double-target experiments designed to test double-shell velocity multiplications, to serve as a diagnostic, and to generate high pressures are possible. A number of important questions remain, however. These include: the effect of multi-millimeter density scale lengths, expected in reactor sized pellets, upon, for example, large amplitude stimulated Brillouin backscatter; a more precise study of illumination symmetry requirements; and finally, the ultimate importance of hydrodynamic instability which may dictate the lowest irradiance possible.

Our conclusion and outlook are best summed up in Fig. 30.

IX. Acknowledgements:

We acknowledge the significant contributions to this work by M. Fink, R. McGill, N. Nocerino, L. Seymour and E. Turbyfill. This work is funded by the U.S. Department of Energy.

References

a. NRC/NRL Resident Research Associate.

b. University of Maryland, College Park, MD.

c. Mission-Research Corp., Alexandria, VA.

1. B.H. Ripin et al., Phys. Rev. Lett. 39, 611 (1977); B.H. Ripin and E.A. McLean, Appl. Phys. Lett. 34, 809 (1979); B.H. Ripin, NRL Memo Report #3864 (1977); D.W. Phillion, W.L. Kruer and V.C. Rupert, Phys. Rev. Lett. 39, 1529 (1977).

2. C.M. Armstrong, et al., J. Appl. Phys. 50, 5233 (1979). B.H. Ripin et al., Phys. Rev. Lett. 34, 1313 (1975).

3. F.C. Young et al., Appl. Phys. Lett 30, 45 (1977).

4. A detailed description of these experimental studies up to Dec. 1978 is given by: B.H. Ripin, R. Decoste, S.P. Obenschain, S.E. Bodner, E.A. McLean, F.C. Young, R.R. Whitlock, C.M. Armstrong, J. Grun, J.A. Stamper, S.H. Gold, D.J. Nagel, R.H. Lehmberg and J.M. McMahon, in Phys. Fluids, to be published (May 1980); also, see NRL Memo Report #3890 (1978), B.H. Ripin, Ed.

5. J.M. McMahon and R.H. Lehmberg, CLEOS/ICF 80', San Diego, CA, pg. 122, Technical Digest, pub. Optical Society of America (1980).

6. S.P. Obenschain, E.A. McLean and S.H. Gold (to be published).

7. E.A. McLean, et al., (to be published).

8. B.H. Ripin et al., Phys. Rev. Lett. 43, 350 (1979).

9. J.P. Anthes, M.A. Palmer, M.A. Gusinow and M.K. Matzen, Appl. Phys. Lett. 34, 841 (1979).

10. R. Decoste, et al., Phys. Rev. Lett. 42, 1673 (1979).

11. J.P. Anthes, M.A. Gusinow and M.K. Matzen, Phys. Rev. Lett. 41, 1300 (1978); M. Gusinow et al., Appl. Phys. Lett. 33, 800 (1978).

12. R. Decoste et al., Bull. Am. Phys. Soc. 24, 1074 (1979).

13. J. Grun, B.H. Ripin, R. Decoste and S.P. Obenschain, Bull. Am. Phys. Soc 24, 1074 (1979); also, to be published.

14. E.A. McLean, S.H. Gold, J.A. Stamper, S.P. Obenschain, B.H. Ripin and S.E. Bodner, Bull. Am. Phys. Soc. 24, 1075 (1979); also, to be published.

15. S.P. Obenschain, et al. (to be published).

DEVIL vs DEEP BLUE SEA

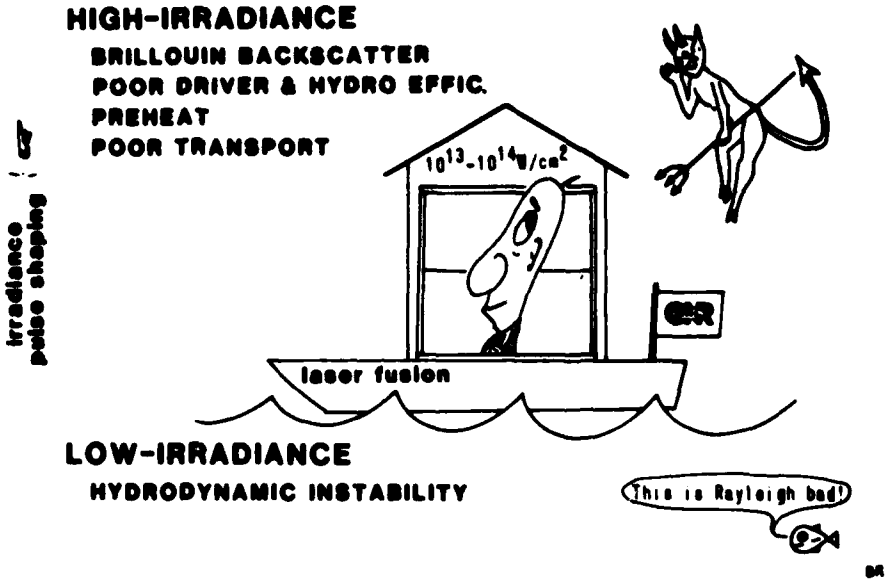

Figure 1

NRL ABLATIVE ACCELERATION EXPERIMENTS

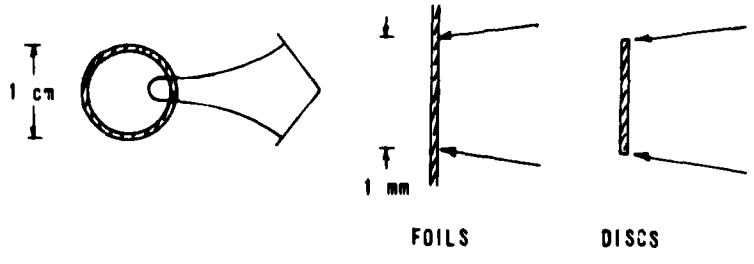

- **OBJECTIVE**

  ABLATIVELY ACCELERATE TARGET STABLY TO 2×10^7 cm/sec (20 J/μg) WITH GOOD EFFICIENCY ON A LOW ADIABAT.

- **REGIME**

  LONG PULSES, 10^{13}-10^{14} W/cm^2, λ-1.05 μm

Figure 2

ABLATIVE ACCELERATION

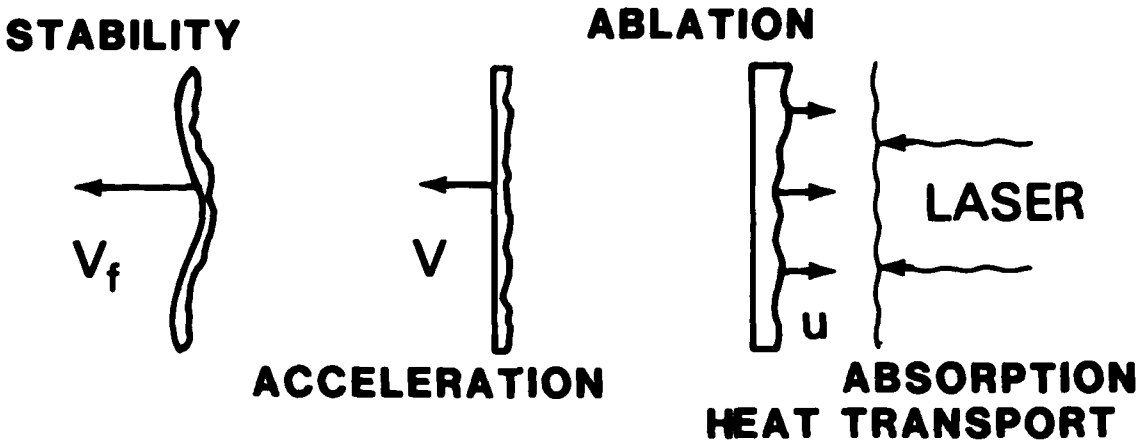

Figure 3

PHAROS II LASER

- Nd-PHOSPHATE GLASS, 1.054 μm

  500-1000 J, 3 nsec

- FOCAL SPOT UNIFORM 1 mm DIA

  $I = 10^{13} - 10^{14}$ W/cm^2

Figure 4

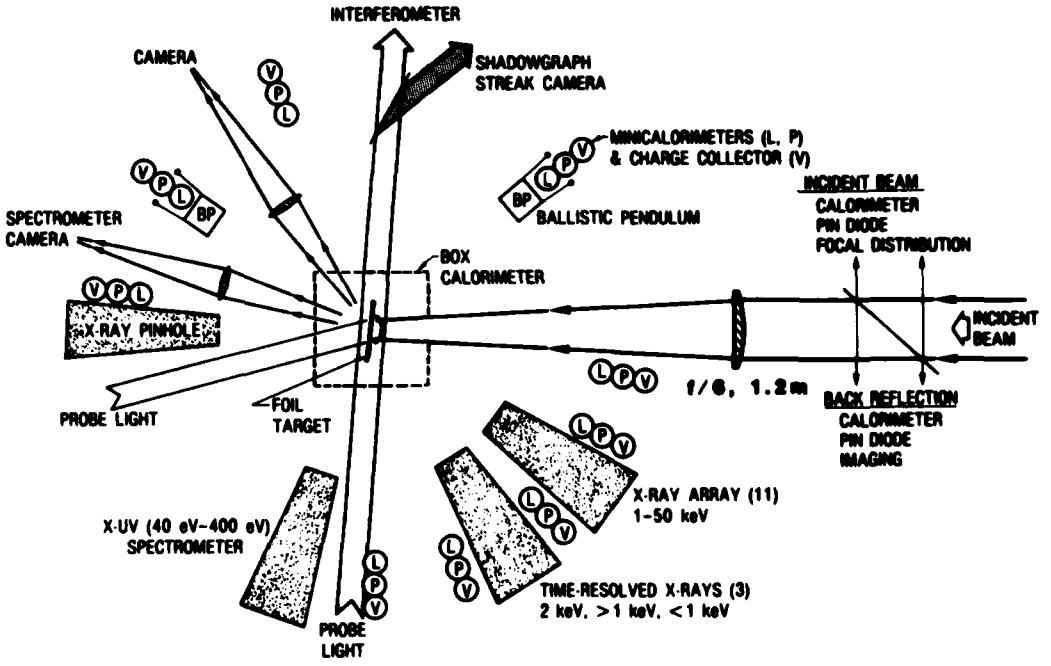

Figure 5

ABSORPTION SUMMARY

W/cm^2	3×10^{12}	1×10^{13}	7×10^{14}
ABSORPTION	90%	80%	55%
ENERGY BALANCE	———	100 ± 10 %	———

Figure 6

X-RAY SPECTRA IRRADIANCE DEPENDENCE

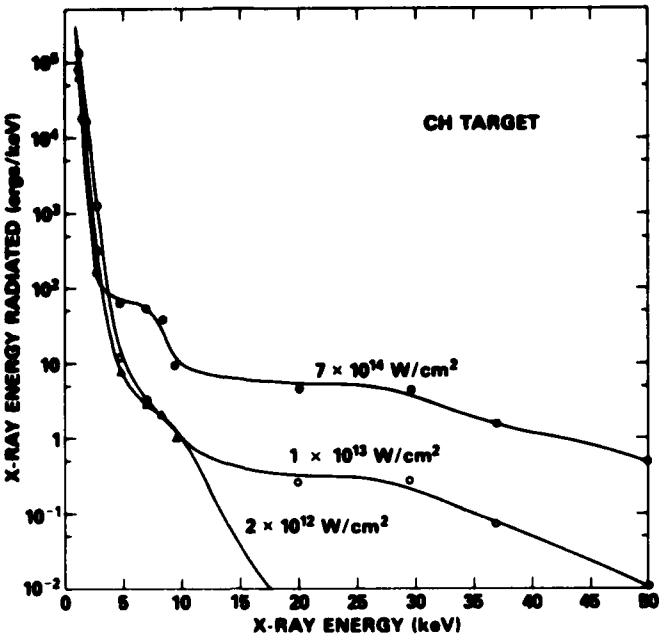

Figure 7

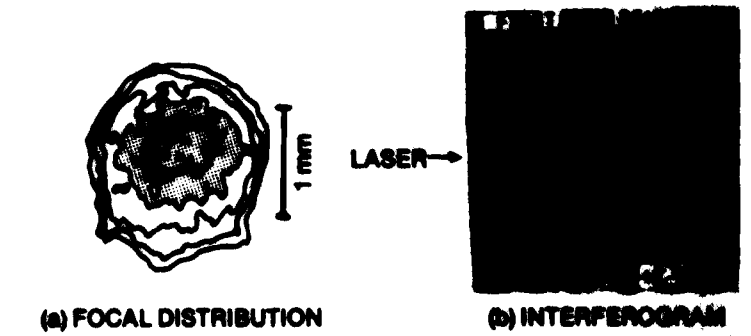

Fig. 8 - Optical views of accelerating target

MEASUREMENT OF ABLATION PARAMETERS

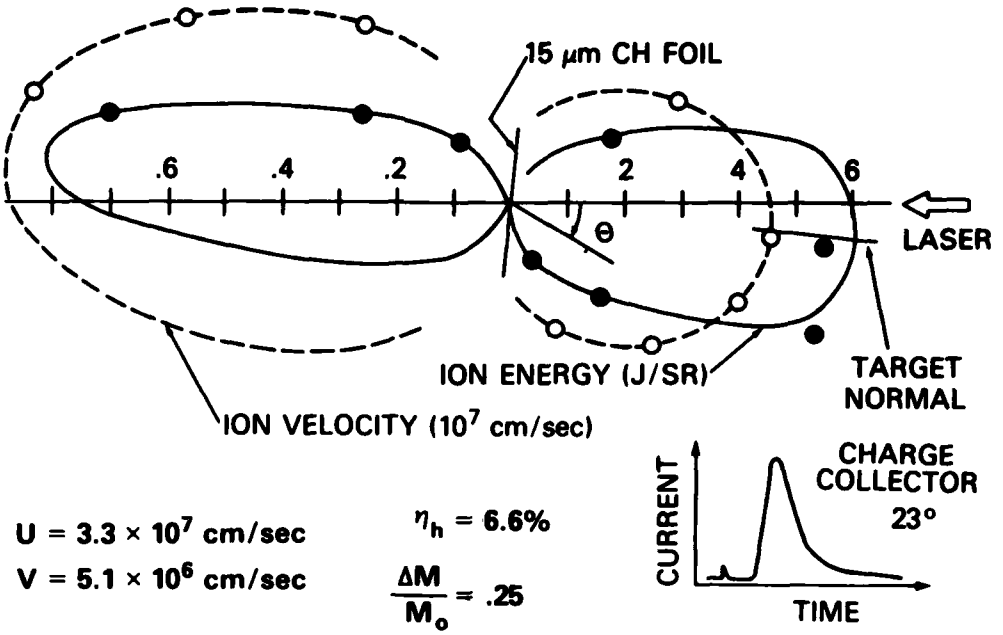

$U = 3.3 \times 10^7$ cm/sec

$V = 5.1 \times 10^6$ cm/sec

$\eta_h = 6.6\%$

$\frac{\Delta M}{M_o} = .25$

Figure 9

ABLATIVE ACCELERATION: EXPERIMENT AND THEORY

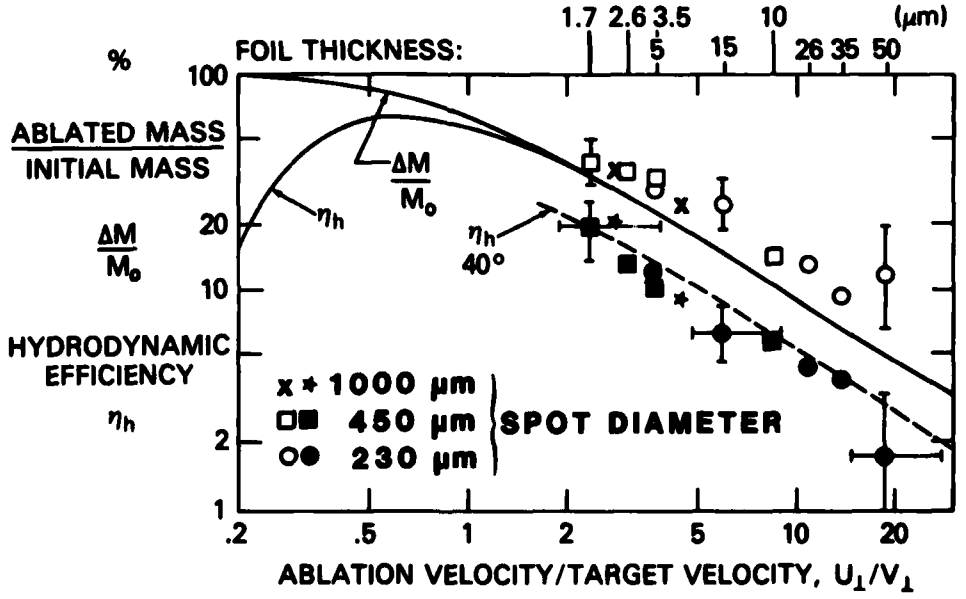

Figure 10

ABLATION VELOCITY vs LASER SPOT SIZE

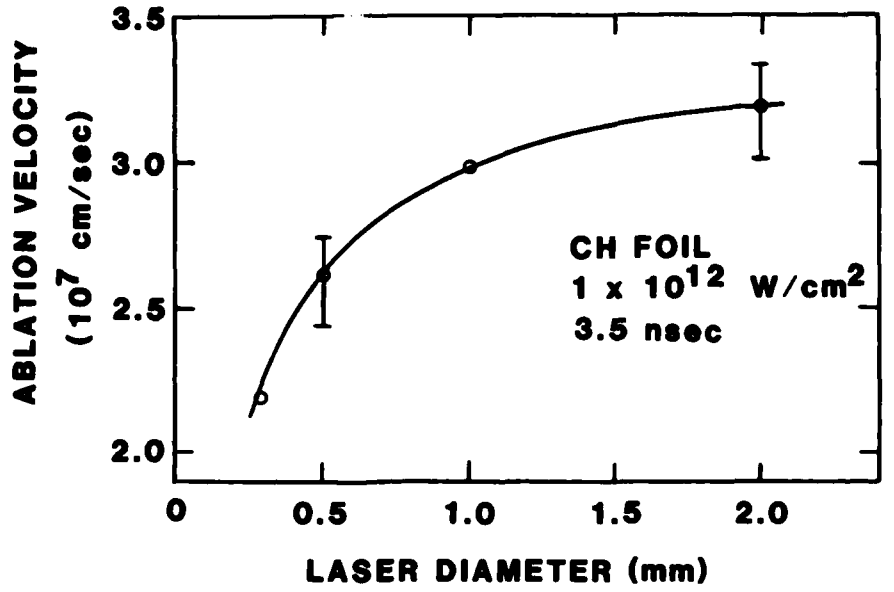

Figure 11

ABLATION VELOCITY vs IRRADIANCE

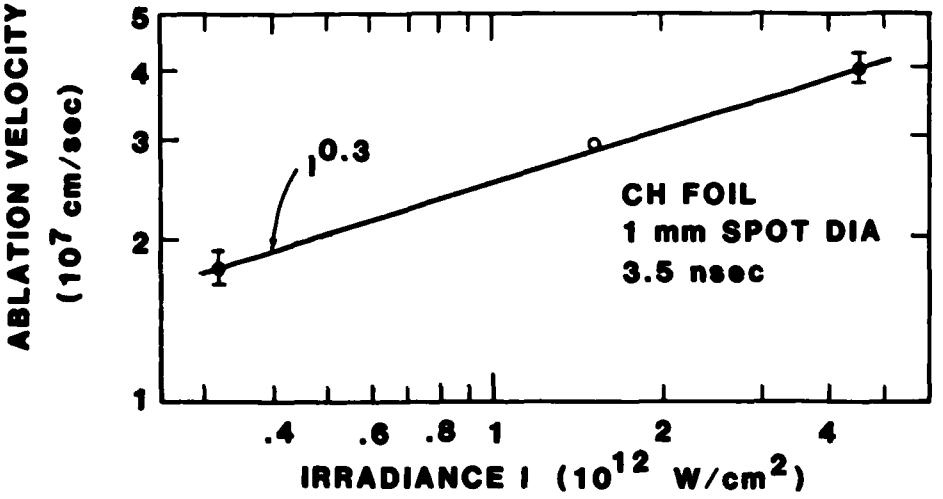

Figure 12

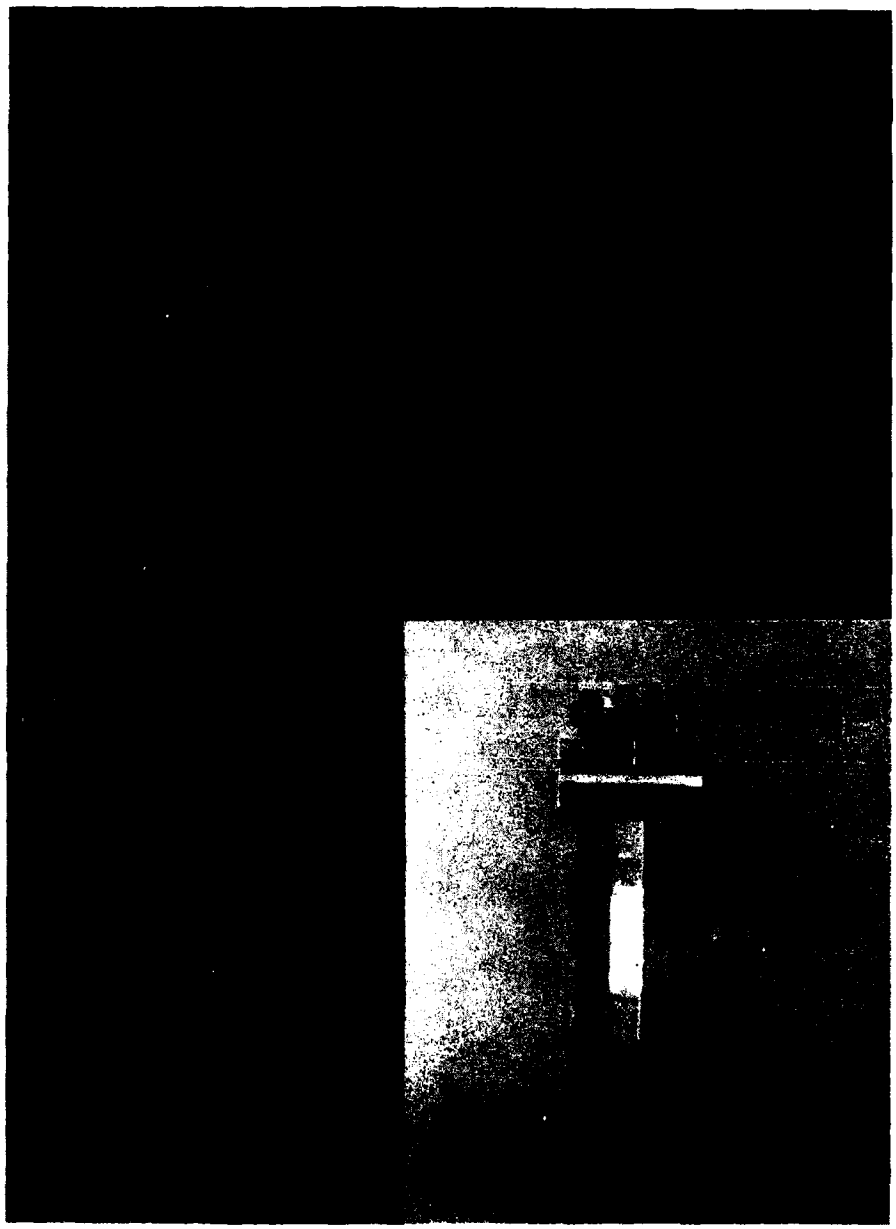

Figure 13

BALANCE TARGET - BLOWOFF MOMENTUM

7×10^{12} W/cm^2
SPOT DIAMETER $\simeq 425$ μm
12 μm CH FOIL TARGET
$\tau_\ell = 3$ nsec

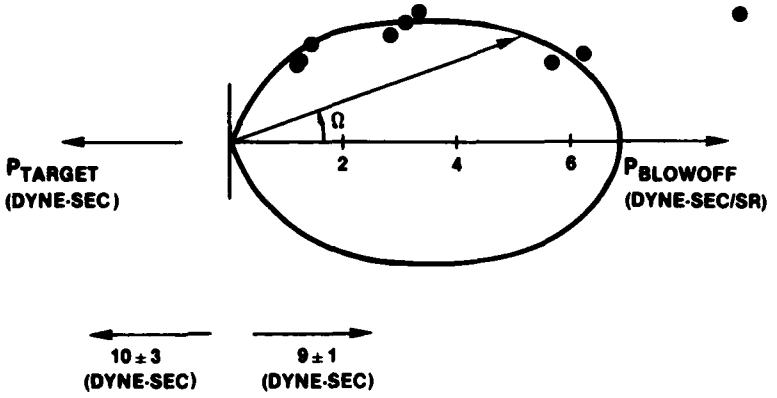

Figure 14

PRESSURE vs INTENSITY

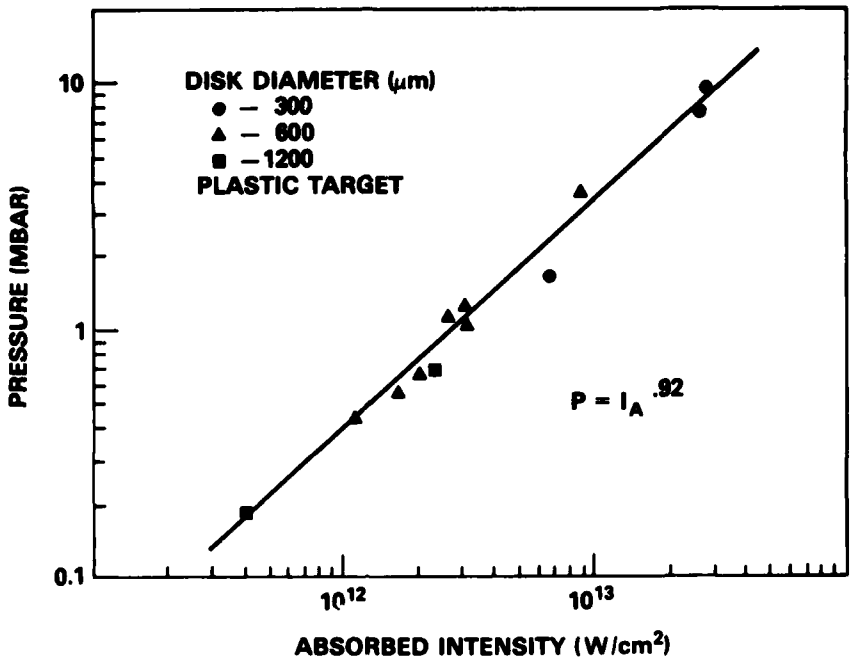

Figure 15

LAYERED TARGET TECHNIQUE

$$\frac{\text{AL LINE RADIATION}}{\text{CH EMISSION}}\Big|_{\text{1-2 keV}} \gg 1$$

UPON BEING HEATED TO A FEW HUNDRED eV

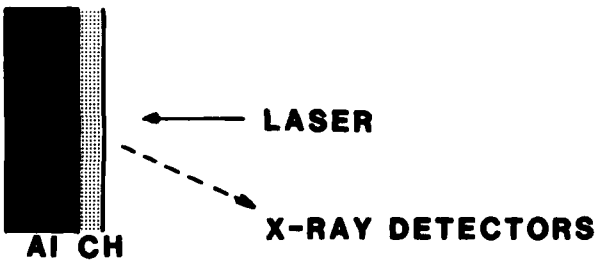

☞ AXIAL HEAT FLOW AND ABLATION DEPTH

Figure 16

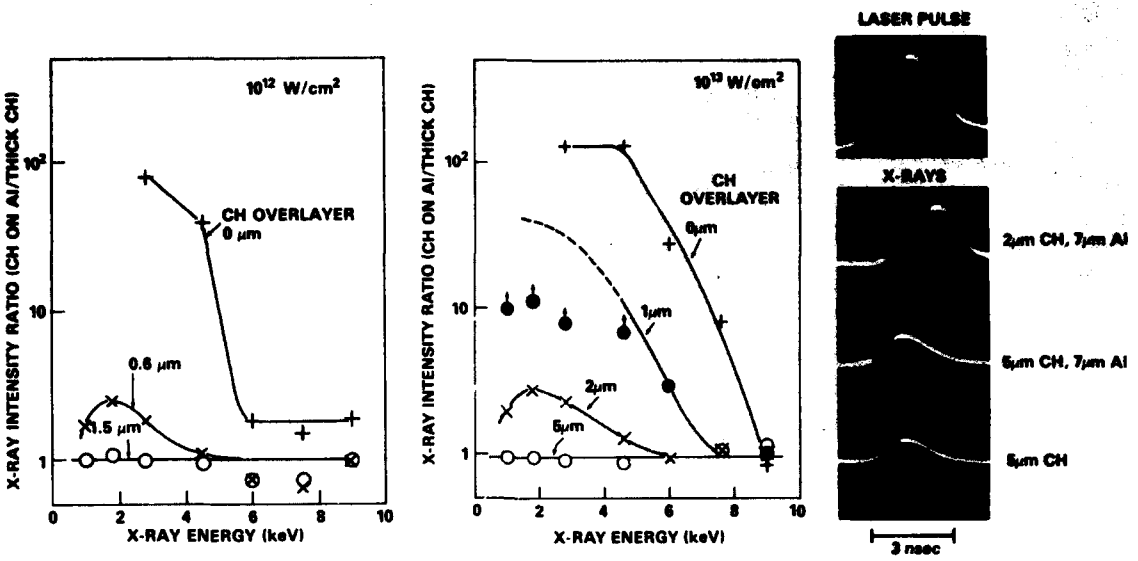

Fig. 17 - Axial thermal conduction

TEMPERATURE MEASUREMENT ON BACKSIDE OF TARGET

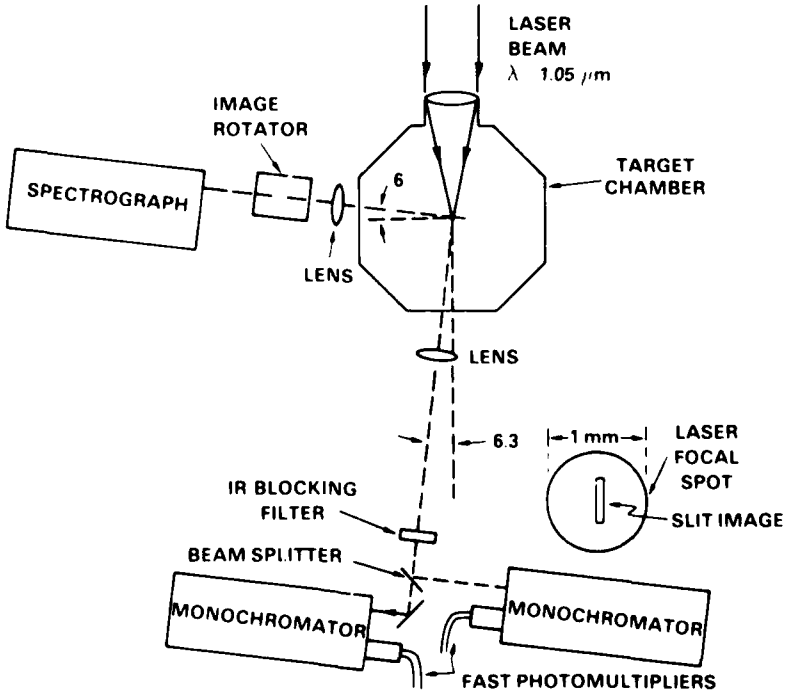

Figure 18

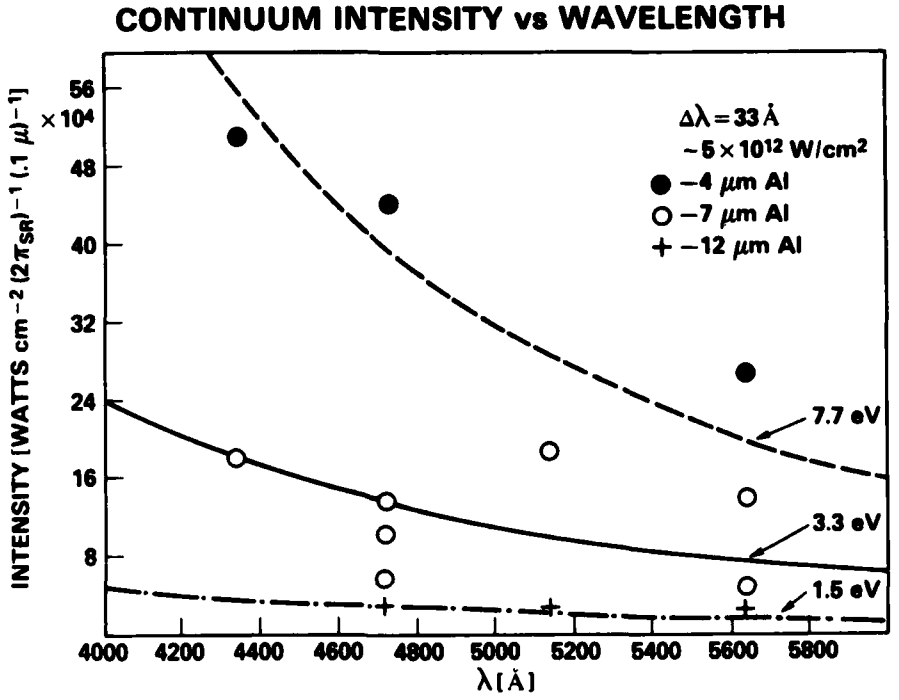

Figure 19

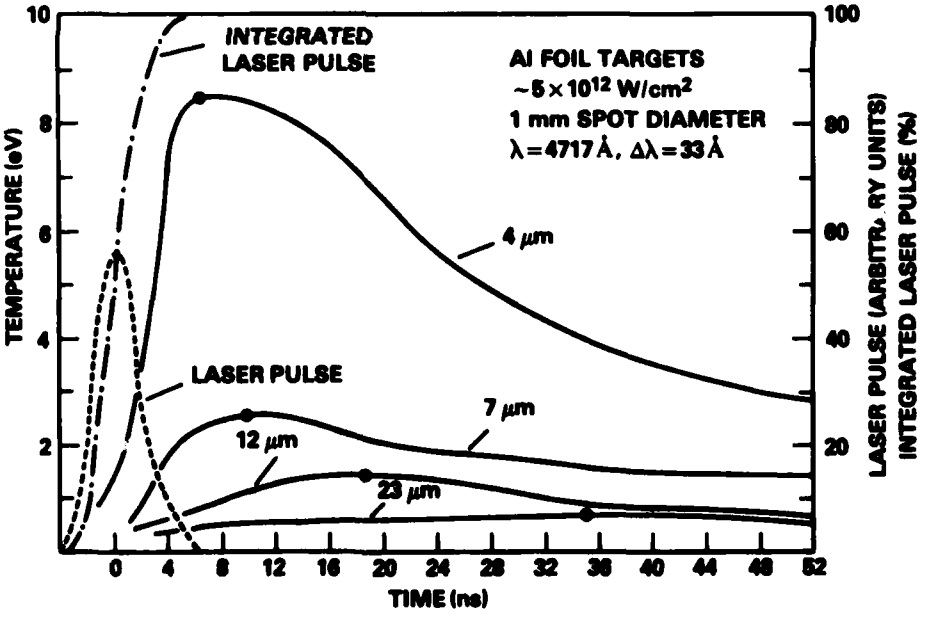

Figure 20

ILLUMINATION SYMMETRY

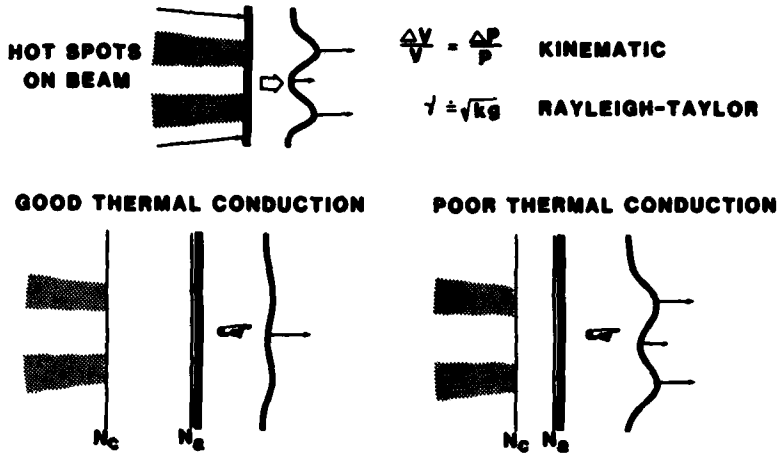

Figure 21

DOPPLER REAR SURFACE VELOCITY PROFILES

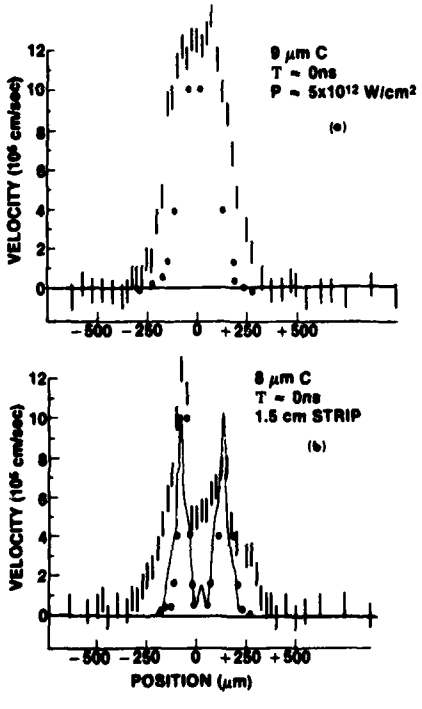

Figure 22

VELOCITY, X-RAY, and INTENSITY PROFILES
(1 mm targets)

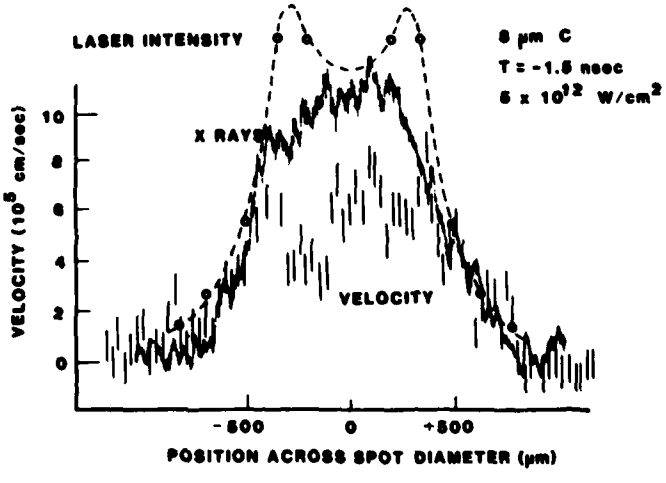

Figure 23

DOUBLE-TARGET EXPERIMENTS

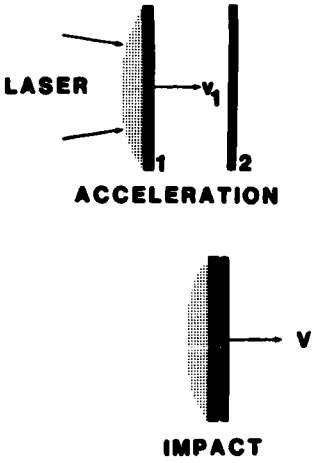

- o VELOCITY MULTIPLICATION (analogue to double shell pellet)
- o DIAGNOSTIC TOOL
- o HIGH-PRESSURE GENERATION

Figure 24

DIAGNOSTIC OF PRESSURE DISTRIBUTION

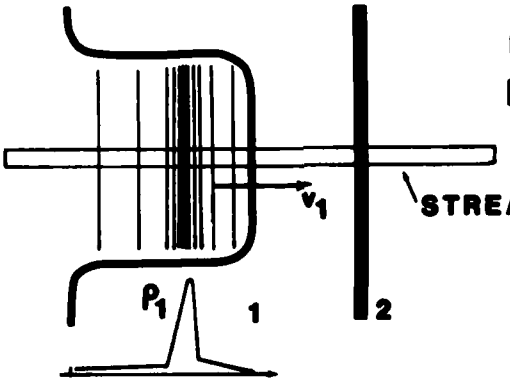

PRESSURE

$P_1(t) \doteq \rho_1 v_1^2 \doteq m_2 \dot{v}_2$

STREAK CAMERA SLIT

Figure 25

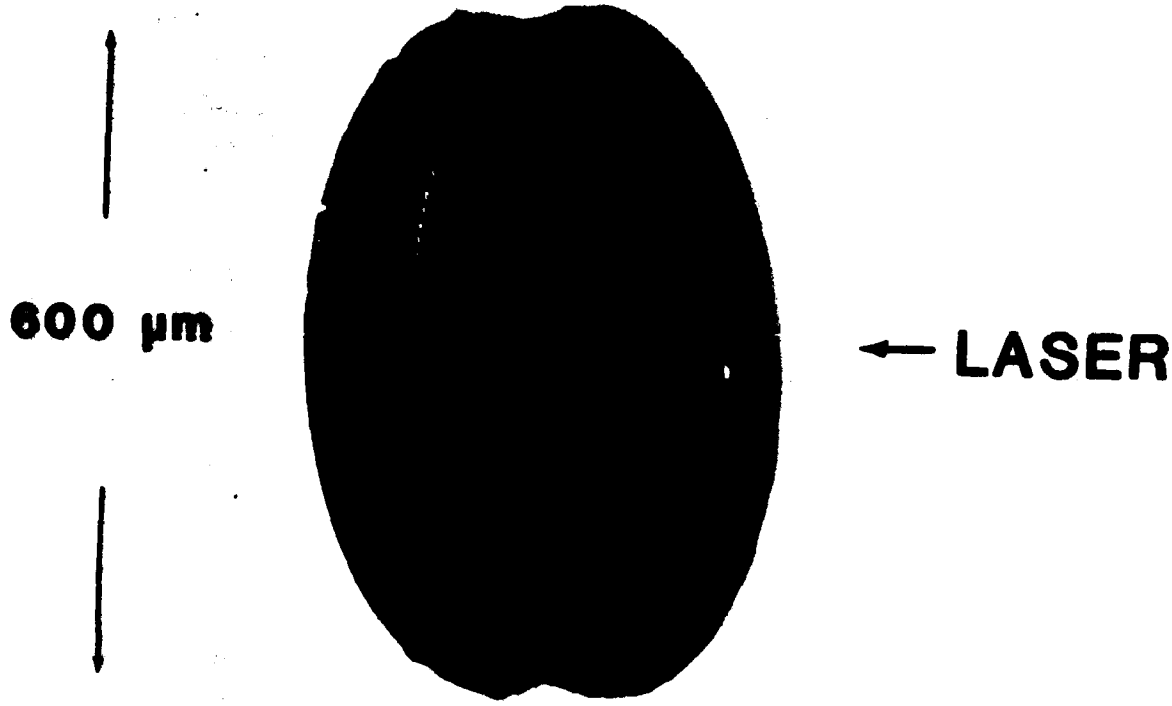

Fig. 26 - Double-disc target

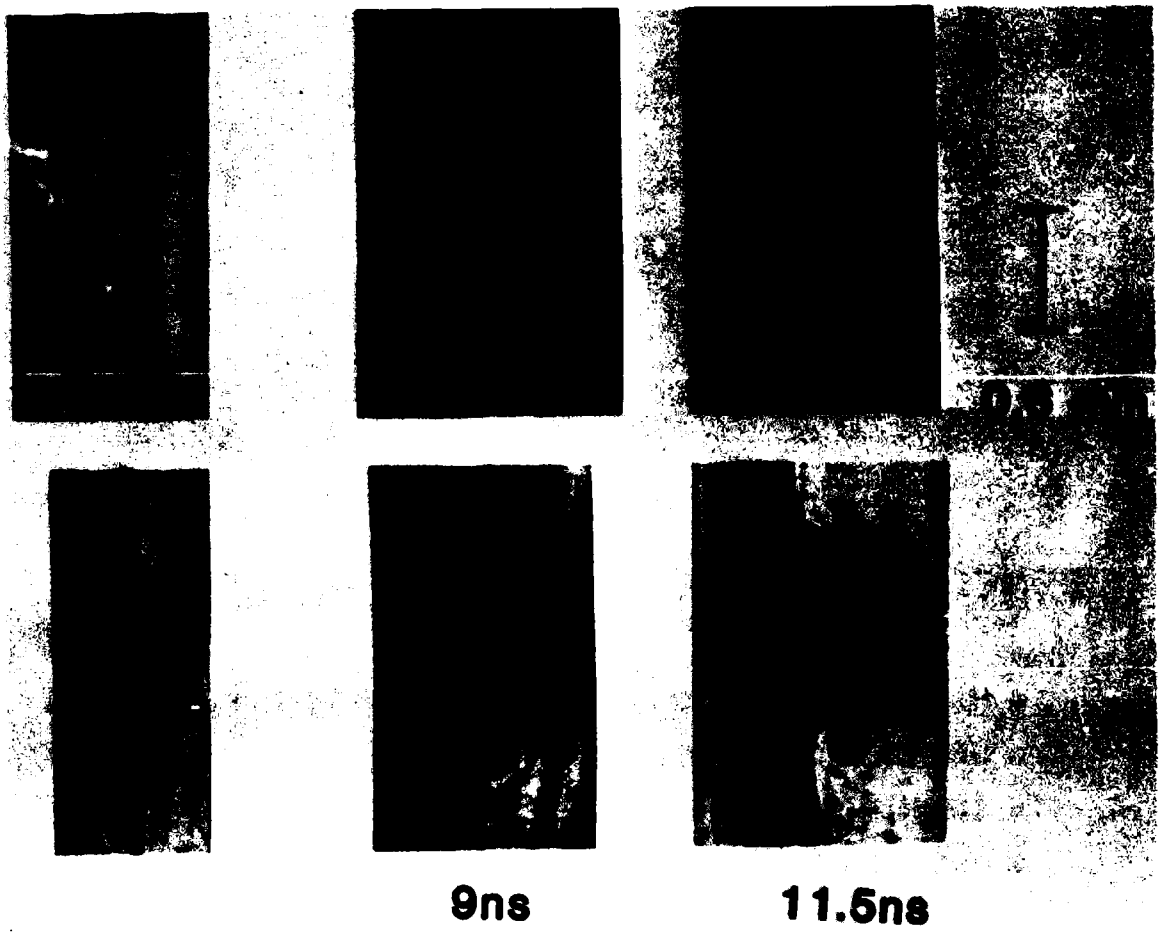

Fig. 27 - Double foil results

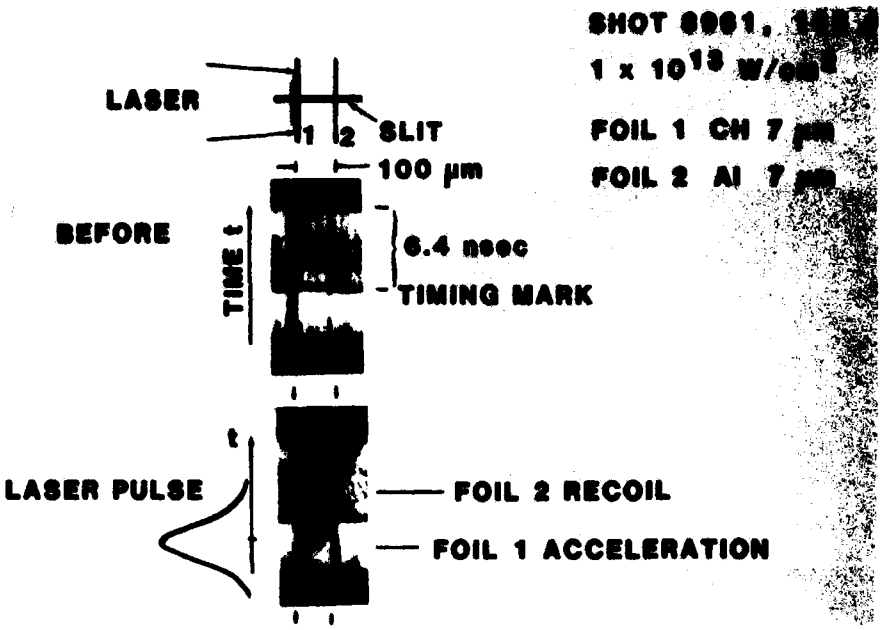

Fig. 28 - Double-foil experiments

BENEFITS OF LOW-IRRADIANCE APPROACH

- o HIGH DRIVER, ABSORPTION and HYDRO EFFICIENCIES
- o UNSHAPED PULSES
- o SIMPLE TARGETS
- o PHYSICS LOOKS GOOD SO FAR
  - absorption thermal
  - preheat low
  - ablative acceleration works
  - small scale nonuniformities wash out
  - double targets possible

- ? LONG SCALELENGTH EFFECTS
- ? ILLUMINATION SYMMETRY REQUIREMENTS
- ? RAYLEIGH-TAYLOR INSTABILITY

Figure 29

CONCLUSION

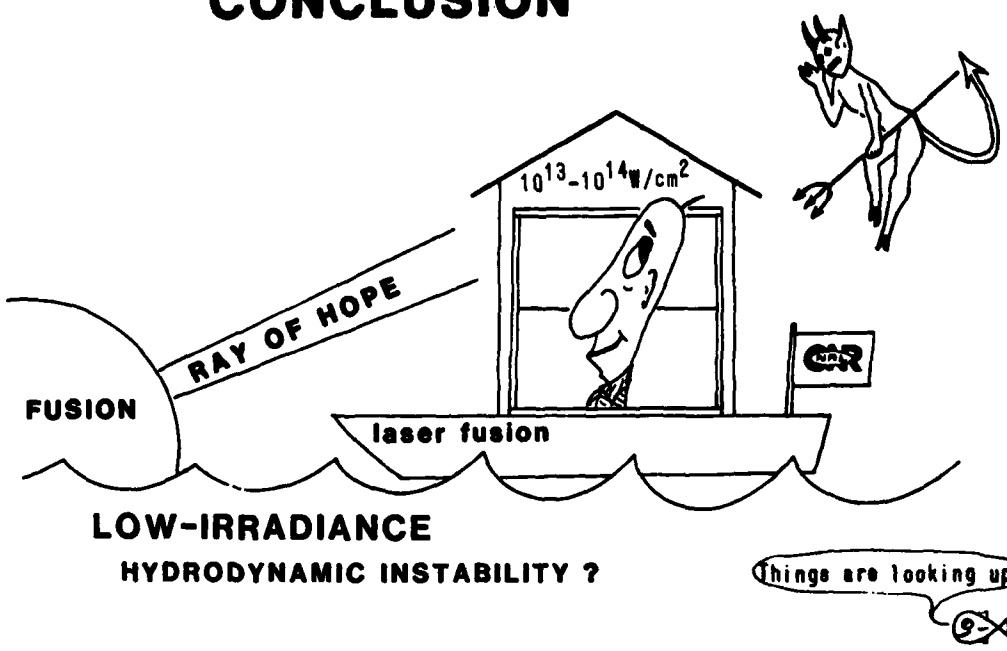

Figure 30

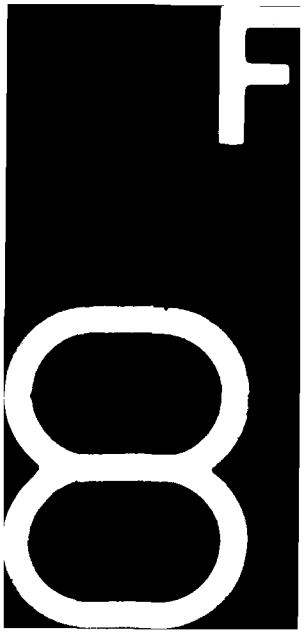
8F